MIT Libraries | DSpace@MIT

MIT Open Access Articles

Effects of Solute and Vacancy Segregation on Migration of a/4<111> and a/2<100> Antiphase Boundaries in Fe_3Al

The MIT Faculty has made this article openly available. ***Please share*** how this access benefits you. Your story matters.

Citation: Koizumi, Yuichiro, Samuel M. Allen, and Yoritoshi Minamino. "Effects of Solute and Vacancy Segregation on Migration of a/4#111# and a/2#100# Antiphase Boundaries in Fe_3Al." Acta Materialia 57.10 (2009): 3039–3051. Web.

As Published: http://dx.doi.org/10.1016/j.actamat.2009.03.012

Publisher: Elsevier B.V.

Persistent URL: http://hdl.handle.net/1721.1/70086

Version: Author's final manuscript: final author's manuscript post peer review, without publisher's formatting or copy editing

Terms of use: Creative Commons Attribution-Noncommercial-Share Alike 3.0

Massachusetts Institute of Technology

Effects of Solute and Vacancy Segregation on Migration of *a*/4<111> and *a*/2<100> Antiphase Boundaries in Fe_3Al

Yuichiro Koizumi[a, b], Samuel M. Allen[a], Yoritoshi Minamino[b]

[a] *Department of Materials Science and Engineering, Massachusetts Institute of Technology, Cambridge, MA, USA*

[b] *Department of Adaptive Machine Systems, Osaka University, 2-1 Yamadaoka, Suita, Osaka, Japan*

Abstract

Effects of segregation of solute atoms and vacancies on migration of *a*/4<111> and *a*/2<100> antiphase domain boundaries (APDBs) in stoichiometric Fe_3Al at various temperatures are studied using a phase-field model [Koizumi et al., Acta Mater. 2008;56:5861] based on the Bragg-Williams approximation and kinetic parameters determined from experimental data. Boundary mobilities (*M*) were measured from the boundary velocity of shrinking circular antiphase domains (APDs). In the case of *a*/4<111> APDBs, solute atmospheres follow the APDB until the APD vanishes by shrinking to zero radius, and therefore the *M*s are always smaller than the intrinsic boundary mobilities because of the solute-drag effect. The *M* of *a*/4<111> APDBs can be enhanced by up to 60% by vacancy segregation. On the other hand, the *M* of *a*/2<100> APDBs is enhanced by only a few percent. The *a*/2<100> APDBs are observed to break away from the solute atmosphere during the course of the shrinking. The *M* increases by up to 40 % associated with the breakaway, and becomes equal to the intrinsic boundary mobilities even though slight depletion and segregation of Al-atoms remain ahead and behind the migrating boundary, respectively.

Keywords: Interface segregation; Phase-field models; Vacancies; Antiphase domain; Long-range ordering

1. Introduction

Fe_3Al alloys have been developed as high-temperature structural materials [1]. The mechanical properties of Fe_3Al are closely related to the ordered arrangement of Fe atoms and Al atoms forming $D0_3$- and $B2$-ordered structures depending on the chemical composition and temperature [2]. Antiphase domains (APD) which are microstructural features in ordered phases have significant influences on plastic properties by affecting dislocation motion [3-5]. Recently, it was reported that pseudo-elasticity is caused in Fe_3Al by the interaction between APD boundaries (APDBs) and dislocations [6-10]. The magnitude of pseudoelasticity greatly depends on the APD size, and therefore the control of APD size and prediction of their stability are increasingly important. The author's experimental work [11] implied that the effects of inhomogeneity of lattice defects such as vacancies, solute atoms and dislocations are important for understanding accurately the kinetics of APD formation and growth. For instance, when an Fe_3Al alloy is rapidly quenched from a temperature above its order-disorder transition temperature (T_c) and annealed at a temperature below T_c, the APD growth is enhanced by the excess vacancies introduced by the quenching [11]. The enhancement of APD growth tends to be more significant as the difference between the quenching temperature and the annealing temperature increases. However, when the difference between the temperatures is extremely large, the excess vacancies tend to aggregate to form dislocation loops. Such dislocation loops are supposed to become sinks for the remaining excess vacancies and make the vacancy concentration inhomogeneous. APDB migration may be affected by such an inhomogeneity of vacancies.

In the companion paper [12], the segregation of solute atoms and vacancies on stationary planar APDBs in Fe-Al alloys near the stoichiometry Fe_3Al (Fe−22~28at.%Al) was studied using a phase-field model based on the Bragg-Williams approximation. There are two types of APDBs in the $D0_3$-structure. One has the phase-shift vector of $a/2<100>$ and the other has that of $a/4<111>$, where a is the lattice parameter. The former can be formed in only $D0_3$-structure whereas the latter can be formed in both $B2$- and $D0_3$-structures. The former and the latter are denoted as $D0_3$-APDB and $B2$-APDB respectively in the present study.

Fe-atoms and vacancies segregate to $D0_3$-APDB in crystals with stoichiometric composition (Fe−25at.%Al) and with the Fe-rich composition, whereas both tend to be depleted in Al-rich crystals. On the other hand, both Fe-atoms and vacancies segregate on $B2$-APDBs in all compositions studied. The vacancy concentration at the center of an APDB can be up to 80 % larger than that in matrix. Although the effects of vacancy segregation on APDB energy and thickness are negligibly small, it is anticipated that the migration of APDB can be significantly affected by vacancy segregation as well as by solute segregation because the boundary mobility is expected to be proportional to the vacancy concentration in materials where atoms diffuse via vacancy mechanisms.

Solute-drag effects on grain boundary migration have been studied for a long time [13-22]. Lücke et al. [13] were the first who suggested the solute-drag effect considering an attraction of solute atoms to a grain boundary. Cahn [14] classified the solute-drag into high-velocity (high-driving force) and low-velocity (low-driving force) extremes. Hillert developed a free energy dissipation theorem for migrating boundaries [15, 16]. Cha et al. [17] demonstrated their phase-field model for grain boundary migration is consistent with both Cahn's solute-drag theory and Hillert's free energy dissipation theorem. Later, Hillert proved that the solute-drag theory and the energy dissipation theorem are equivalent [18]. Mendelev et al. developed a theory of

solute-drag in a regular solution by expanding Cahn's solute drag theory of an ideal solution [19]. Kim and Park examined the effects of impurity-drag on shrinking circular boundaries [20]. Solute-drag at migrating APDBs in Fe_3Al was studied by Krzanowski and Allen both theoretically and experimentally using their experimental data of APD growth in Fe_3Al [21, 22]. They predicted theoretically that the transition from low driving-force extreme to high driving-force extreme occurs during APD growth and demonstrated their predictions are relatively in good agreement with the experimentally observed APD growth. However, their model neglects the effects of coupling of long-range-order (LRO) and composition, and can be improved by taking it into account [21, 22].

The ability to couple order parameters and composition is one of the advantages of the phase-field model. There has been no study in which phase-field method is used for evaluating the effect of segregation on the APDB migration, nor has there been any study on the effect of inhomogeneous vacancy distribution on boundary migration. In the present study, the effects of solute and vacancy segregation on migration of APDB are studied by simulating shrinking circular APDs in a stoichiometric vacancy-containing Fe_3Al. The effects of offstoichiometry on migration kinetics will be presented in a future publication.

2. Model

2.1 Cahn-Hilliard, Allen-Cahn equations and mobilities

The description of order parameters and free energy in vacancy-containing Fe_3Al was detailed in the companion paper [12]. The definition of the free energy is described briefly in the Appendix for convenience. In order to simulate the temporal change of order parameter fields, the formalism of the Cahn-Hilliard [23] and Allen-Cahn [24] equations require careful consideration. When the mobilities are functions of vacancy concentration (c_v), the Cahn-Hilliard equation for the Al concentration (c_{Al}) field is written as

$$\frac{\partial c_{\mathrm{Al}}}{\partial t} = \nabla \cdot \left\{ \beta_{\mathrm{Al}}^{\mathrm{dep.}}(c_{\mathrm{v}}, T) \nabla \left(\frac{\delta F}{\delta c_{\mathrm{Al}}} \right) \right\} = \nabla \beta_{\mathrm{Al}}^{\mathrm{dep.}}(c_{\mathrm{v}}, T) \cdot \nabla \left(\frac{\delta F}{\delta c_{\mathrm{Al}}} \right) + \beta_{\mathrm{Al}}^{\mathrm{dep.}}(c_{\mathrm{v}}, T) \nabla^2 \left(\frac{\delta F}{\delta c_{\mathrm{Al}}} \right) \quad (1)$$

where t is the time, $\beta_{\mathrm{Al}}^{\mathrm{dep.}}(c_{\mathrm{v}}, T)$ is the c_{v}-dependent phase-field mobility for c_{Al} and F is the free energy of the system. The β_{Al} that is independent of c_{v} (hereafter denoted as $\beta_{\mathrm{Al}}^{\mathrm{indep.}}(T)$) is given by the Nerst-Einstein equation [25]

$$\beta_{\mathrm{Al}}^{\mathrm{indep.}}(T) = \tilde{D}(T) \Big/ \left(\frac{1}{V_{\mathrm{m}}} \frac{\partial^2 F(T)}{\partial c_{\mathrm{Al}}^{\ 2}} \right) \quad (2)$$

where T is the temperature, R is the gas constant, V_{m} is the molar volume and $\tilde{D}(T)$ is the interdiffusivity at temperature T. Experimental data for $\tilde{D}(T)$ are available in the literature [26]. Assuming that the mobility is proportional to c_{v}, the c_{v}-dependent mobility, $\beta_{\mathrm{Al}}^{\mathrm{dep.}}(c_{\mathrm{v}}, T)$, can be written as

$$\beta_{\mathrm{Al}}^{\mathrm{dep.}}(c_{\mathrm{v}}, T) = \left(\frac{c_{\mathrm{v}}}{c_{\mathrm{v}}^{\mathrm{eq}}(T)} \right) \cdot \tilde{D}(T) \Big/ \left(\frac{1}{V_{\mathrm{m}}} \frac{\partial^2 F(T)}{\partial c_{\mathrm{Al}}^{\ 2}} \right) \quad (3)$$

where $c_{\mathrm{v}}^{\mathrm{eq}}$ is the equilibrium vacancy concentration at temperature T and given by

$$c_{\mathrm{v}}^{\mathrm{eq}}(T) = \exp\left(\frac{S_{\mathrm{F}}}{k_{\mathrm{B}}} \right) \cdot \exp\left(\frac{-H_{\mathrm{F}}}{k_{\mathrm{B}} T} \right) \quad (4)$$

where S_{F} is the vacancy formation entropy and H_{F} is the vacancy formation enthalpy. Experimental data of S_{F} and H_{F} are also available in the literature [27, 28].

The Allen-Cahn equation for the case of the c_{v}-dependent ordering mobilities can be written as

$$\frac{\partial \eta}{\partial t} = -\alpha^{\mathrm{dep.}}(c_{\mathrm{v}}, T) \cdot \frac{\delta F}{\delta \eta} \quad (5)$$

where $\alpha^{\mathrm{dep.}}(c_{\mathrm{v}}, T)$ is the ordering mobility which is the function of c_{v} and T.

Kirkaldy [29] suggested an equation for deriving the ordering mobility for Allen-Cahn equation as,

$$\alpha^{\mathrm{indep.}}(T) = \tilde{D}(T) \left(1 - \frac{T}{T_{\mathrm{c}}} \right)^{0.5} \cdot \frac{1}{\kappa} \quad (6)$$

where T_{c} is the order-disorder transition temperature for the LRO of interest and κ is the gradient

energy coefficient. However, this equation was derived from only dimensional analysis and the physical meaning of this equation is not clear. This equation implies that the mobility vanishes as the temperature approaches T_c. This conflicts with the experimental observations of APD growth in Fe_3Al in which the APD growth rate did not decrease even where the temperature approaches T_c within 10 K [22]. Alternatively, based on Hillert's discussion of ordering kinetics [30], the ordering mobility can be derived as

$$\alpha^{\text{indep.}}(T) = \frac{\tilde{D}(T)}{k_B T d^2} c_{Al}(1 - c_{Al}) \tag{7}$$

where k_B is Boltzmann's constant and d is the interplanar distance. Neither Eq. (6) nor Eq. (7) has been justified satisfactorily. Oki et al. [31] have reported the temporal change of LRO parameters during order-order relaxation (i.e. relaxation from lower degree of order to higher degree of order within a temperature range where the ordered phase remains stable) by isothermally annealing an Fe_3Al alloy quenched from a temperature between the annealing temperature and the $B2/D0_3$ transition temperature, $T_c^{B2/D0_3}$. Their report is the only one in which changes of both $B2$-LRO (η_{B2}) and $D0_3$-LRO (η_{D0_3})* without the influence of APD growth are available. Park et al. [32] have measured order-order relaxation in Fe_3Al by an in-situ synchrotron X-ray diffraction experiment. However, only one of the two types of LRO was measured at each temperature in their experiment.

The values of $\alpha^{\text{indep.}}$ for $B2$-LRO ($\alpha_{\eta_{B2}}^{\text{indep.}}$) and $D0_3$-LRO ($\alpha_{\eta_{D0_3}}^{\text{indep.}}$) at 656 K were determined by fitting the calculated change in the LROs to Oki et al.'s experimental data. The values of $\alpha_{\eta_{B2}}^{\text{indep.}}$ and $\alpha_{\eta_{D0_3}}^{\text{indep.}}$ obtained are 1.2×10^{-12} $m^2N^{-1}s^{-1}$ and 1.2×10^{-11} $m^2N^{-1}s^{-1}$, respectively. Oki et al. [31] reported the activation energy of 193 kJ/mol for both $D0_3$- and $B2$-ordering. This value was obtained by conducting the same type of measurement of ordering at 636 K and analyzing the temperature dependences of the ordering rate. Since the temperature range of the experiment is narrow, there

* Since quite a few parameters are defined, $B2$-LRO and $D0_3$-LRO are represented by η_{B2} and η_{D0_3} for clarity in the present study instead of η_1 and η_2 which were used in the companion paper.

may be a large error when estimating the ordering mobilities at temperatures significantly different from those temperatures, although it is probably permissible to extrapolate to relatively close temperatures such as 673 K. Once $\alpha_{\eta_X}^{\text{indep.}}(T)$ is determined, a c_v-dependent mobility ($\alpha_{\eta_X}^{\text{dep.}}(c_v,T)$) is given by

$$\alpha_{\eta_X}^{\text{dep.}}(c_v,T) = \alpha_{\eta_X}^{\text{indep.}}(T)\left(\frac{c_v}{c_v^{\text{eq}}(T)}\right) \tag{8}$$

where η_X represents η_{B2} or η_{D0_3}. Kinetic data for diffusion [26-28] and ordering [31] used in the present study are listed in Table 1. Since various mobilities are employed in the present study, the mobilities are classified in Table 2 for clarity. The meaning of the boundary mobilities, velocities and driving forces in the tables will be explained in the next section.

2.2 Simulation

APDBs with the shape of a quarter circle were formed in a 2D simulation box of 128 pixel × 128 pixel which corresponds to 15 nm × 15 nm. The initial radius of the APDB was set to be 11.2 nm. This initial radius was determined from the size of the simulation box and the width of the equilibrated planar APDB. It is the maximum radius of APD which can be introduced in the box without interference between the APDB and the edge of the simulation box at all the temperatures examined. The initial order parameter profiles across the APDB were assumed to be same as those across the equilibrated planar APDBs which were calculated in the previous study [12]. A zero-flux boundary condition was applied to the edges of the simulation box. This boundary condition enables us to simulate the shrinking of a circular APD by calculating only a quarter circle utilizing the symmetrical property of circles. In order to see the effect of vacancy segregation, simulations with the assumption of c_v-independent mobilities were also performed.

According to a study of vacancy concentration relaxation in a rapidly quenched Fe-25at%Al alloy, the enthalpy for vacancy migration is only 43 kJ mol^{-1} (0.45 eV), and therefore the diffusivity

of vacancies (D_V) is expected to be extremely large compared with those of Fe- and Al-atoms. For instance, the D_V estimated from the vacancy migration enthalpy is larger than interdiffusivity by factors of 2×10^5 and 1×10^3 at 673 K and 873 K, respectively. For numerically calculating the evolution of vacancy and solute fields by calculus of finite differences, the time step must be set small enough to keep the calculation stable. The time step required is inversely proportional to the diffusivity of the fastest diffuser, and therefore the computation time for a system with vacancies become unrealistically compared with that for a vacancy-free system. In order to avoid this difficulty, the c_V was relaxed so that the diffusion potential for vacancies becomes uniform throughout the simulation box, keeping the total amount of vacancies constant at each time step. c_{Al} was evolved using the calculus of finite differences. This methodology is applicable to the system investigated in this study where the size of simulation box is as small as 30 nm and there is no long-range vacancy concentration gradient.

3. Results

Fig. 1 shows the evolution of LRO (a, b, c, d), c_v (e, f, g, h) and c_{Al} (i, j, k, l) around the shrinking *B*2-APD at 673 K by way of example. The APD shrank with time and finally vanished before 1000 ks. The aluminum depletion and the vacancy segregation followed the APDB until the APD vanished. No significant change was observed in the magnitude and the width of the aluminum and vacancy atmospheres. Fig. 2 shows snap-shots of the shrinking $D0_3$-APD at 673 K. The APDB is broad (Fig 2a) and the Al-depletion and the vacancy-segregation at 1×10^3 s were moderate (Fig. 2e and 2i) compared to the case of *B*2-APD (Fig. 1). The Al-depletion atmosphere and vacancy-segregation atmosphere become broader as the APD shrinks (Fig. 2b, 2f, 2j) and finally the APD was separated from the broadened solute depletion atmospheres.

Fig. 3 shows the changes in the APD radii (r) as a function of annealing time at 673 K. Four

cases of $B2$-APD with c_v-dependent mobilities, $B2$-APD with constant mobilities, $D0_3$-APD with c_v-dependent mobilities and with c_v-independent mobilities are all indicated together. The radius change before 60 ks is enlarged in Fig.3b. The shrinking rates of $D0_3$-APDs are larger than those of $B2$-APDs by more than one order of magnitude. It appears the r decreases with time following a parabolic-law [25]. The radius change of $B2$-APD in the case of c_v-dependent phase-field mobilities is approximately 60 % faster than in the case of c_v-independent mobilities. The effect of vacancy segregation on $D0_3$-APDB migration is much less significant than that on the $B2$-APDB migration. This difference can be attributed to the less significant vacancy segregation on the $D0_3$-APDB than on the $B2$-APDB (Fig. 1 and Fig. 2).

Fig. 4 shows the relationship between the boundary velocity (V) and the curvature ($1/r$). The ranges of the V in Fig. 4a and Fig. 4b are set suitable for seeing the variations of $B2$-APD and $D0_3$-APD, respectively. The small fluctuations arise from numerical error. Overall, the V appears to be proportional to the $1/r$ in all the cases. However, the slope for $D0_3$-APD changes at the point indicated by an arrow, and a gradual increase in the slope is seen for the case of $B2$-APD (Fig.4b). From the slope of the lines connecting the origin of the graph to each point on the curves, the boundary mobilities (M) were evaluated by

$$M = V / (1/r). \tag{9}$$

Hereafter, Ms estimated from the simulation results are denoted as simulated boundary mobility (M^{sim}), and the M^{sim}s for the case of c_v-dependent and c_v-independent phase-field mobilities are denoted as $M_X^{\mathrm{dep.}}$ and $M_X^{\mathrm{indep.}}$ (X represents $B2$ or $D0_3$) as listed in Table 2.

Figs. 5a and 5b show the Ms at 673 K and 773 K respectively as a function of r. After an initial equilibration period, the Ms of $B2$-APDB ($M_{B2}^{\mathrm{dep.}}$ and $M_{B2}^{\mathrm{indep.}}$) are almost constant until the r becomes as small as 4 nm regardless of the c_v-dependence of the phase-field mobilities at both temperatures. Ms increase gradually as r becomes approximately 4 nm, and at smaller radii the

increases accelerate. The rapid increase in the M observed when $r < 1$ nm is due to the influence of the edge of the simulation box which corresponds to the interference between APDBs on opposite sides of the circular APD. At 673 K (Fig.5a), the Ms of $D0_3$-APDB ($M_{D0_3}^{\text{dep.}}$ and $M_{D0_3}^{\text{indep.}}$) increased shortly after the APD started shrinking (indicated by an open arrowhead) regardless of the c_V-dependence of phase-field mobilities. The $M_{D0_3}^{\text{dep.}}$ and $M_{D0_3}^{\text{indep.}}$ become relatively constant when the APD radii fall below approximately 8 nm. This is consistent with the curvature at the point indicated by the arrow in Fig. 4a, and it corresponds to approximately to the time 30 ks in Fig. 2. The effects of c_V-dependence of phase-field mobilities are not negligible. The $M_{B2}^{\text{dep.}}$ is larger than the $M_{B2}^{\text{indep.}}$ by approximately 60% and 30% at 673 K and 773 K respectively, whereas the $M_{D0_3}^{\text{dep.}}$ is larger than $M_{D0_3}^{\text{indep.}}$ by only approximately 8% at most. This difference is consistent with the larger vacancy segregation on $B2$-APDBs than on $D0_3$-APDBs, that is, the c_V's at the center of planar $B2$-APDB and $D0_3$-APDB are larger than those at the matrix by respectively 70% and 10% at 673K, and 50% and 5% at 773 K [12].

The changes of Ms are considered to be associated with the reduction in the solute segregation. For clarifying further the relation between the boundary mobilities, the variations of the c_{Al} profiles were examined. Figs. 6a, 6b and 6c show the profiles of η_{B2}, c_{Al} and c_V across migrating $B2$-APDB at 673 K respectively. The boundary is migrating from right to left. The η_{B2}-profile near the APDB does not exhibit significant change except for the slight increase in its absolute value inside of APD (left side of APDB) seen when r decreases below about 2 nm (Fig.6a). The c_{Al}-profile which was symmetric about to the center of the APDB in the initial condition becomes asymmetric and the interior region of the APD becomes Al-rich as the APD shrinks (Fig. 6b). The c_V-profile also becomes asymmetric as the APD shrinks (Fig. 6c). The vacancy segregation and the Al-atom depletion near the center of the $B2$-APDB do not exhibit significant change until r has shrunk to about 2 nm. The c_{Al} behind the APDB decreases (i.e., Fe-concentration increases) and c_V increases

slightly with decreasing r. This does not happen in the migration of a planar grain boundary considered by Cahn [14]. But a similar decrease in the solute atom concentration behind a circular grain boundary has been observed in a 2D simulation by Kim et al. [20]. This likely arises from the difference in the geometries for 1D simulation and 2D simulation. In 2D simulation, total boundary area decreases with decreasing r so that Fe-atoms and vacancies are shed from the moving circular boundary.

Fig. 7 compares the profiles of η_{D0_3}, c_{Al} and c_v around the $D0_3$-APDB with various r's at 673 K. Both changes of c_{Al}- (Fig.7b) and c_v-profiles (Fig.7c) across $D0_3$-APDBs are quite different from those across $B2$-APDBs (Figs. 6b-c). The Al-atoms tend to segregate in front of the migrating APDB and be depleted behind the boundary (Fig.7b). As the APD radius decreases, the Al-depletion decreases and the Al-segregation increases. Still later, the depletion and segregation of Al atoms abates. A very broad and shallow atmosphere of Al-depletion remains near the initial position of the $D0_3$-APDB whereas no Al-depletion remained in the case of $B2$-APDBs (Fig.6b). Although the depletion and segregation of Al-atoms at the APDB becomes moderate after the APDB has broken away from the Al depletion atmosphere, they do not disappear completely. In accordance with the steep increase in the of M seen to the left of the open arrowhead in Fig. 5a, the $D0_3$-APDB broke away from the initial Al-depletion atmosphere immediately after the APD starts shrinking, and accompanied by Al-segregation and Al-depletion ahead and behind of the shrinking APDB respectively. The accompanying segregation and depletion become weak as the APD shrinks and disappears. The vacancy segregation also becomes weak accompanying the breakaway (Fig.7c). A shallow vacancy segregation atmosphere is left behind the APDB and approximately 40% of segregated vacancies follow the $D0_3$-APDB (Fig.7c) whereas the vacancy segregation at $B2$-APDB does not change much (Fig.6c). The change after the breakaway is quite small in contrast with that of Al-depletion. In Figs 6 and 7, the c_v- and c_{Al}-profiles have been shown only

for the case of c_v-dependent phase-field mobilities. The changes of the c_{Al}- and c_v-profiles for the case of c_v-independent phase-field mobilities (not shown) are almost same as those for the c_v-dependent case. It seems that the background c_{Al} decreases (*i.e.* Fe-concentration increases) behind the moving $D0_3$-APDB as the r decreases (Fig. 7). Although the decrease in APDB area is considered to be partly responsible for this, main reason for this is the breakaway of the APDB from the initial segregation atmosphere and the broadening of the segregation atmosphere in this case.

4. Discussion

The simulation results indicated that the migration of APDBs in Fe_3Al are significantly affected by the segregation of solute atoms and vacancies. The underlying mechanism of the dependence of APDB migration on the segregation should be discussed in terms of the influences of the segregation both on the order parameter mobilities and the driving forces. In the previous study, we found that the effects of vacancy segregation on APDB energy are negligibly small in both cases of $B2$-APDB and $D0_3$-APDB. For instance, the difference of APDB energies for the cases with and without vacancy segregation is less than 1 mJ/m^2 (smaller than the range of numerical error) even for $B2$-APDB at 673 K. The difference would become smaller for $D0_3$-APDB and at higher temperatures. Therefore, the discussion focuses on the effect vacancy segregation on boundary mobilities and on the solute drag effects.

The intrinsic boundary mobility, $M_h^{\text{intrinsic}}$ (h represents η_{B2} or η_{D0_3} in the present study), which is the M without any effect of solute segregation and depletion, can be theoretically derived by Allen-Cahn theory [24] as,

$$M_h^{\text{intrinsic}} = 2\kappa_h\alpha_h \tag{10}$$

where κ_h is the gradient energy coefficient and α_h is the phase-field mobility for order parameter h.

If there is no segregation and the profile of order parameter across the APDB does not deviate from that of a stationary planar APDB, the M evaluated by Eq. (9) from the $V-1/r$ relation should be equal to the $M_h^{\text{intrinsic}}$.

Fig. 8 compares the Ms evaluated from the simulation results (M^{sim}) with theoretically estimated $M_h^{\text{intrinsic}}$ values in the temperature range from 673 K to 873 K. Experimental values of Ms measured by in-situ TEM observation [33] are also shown. The M^{sim}s of $B2$-APDB for the cases of c_{v}-dependent and c_{v}-independent ordering mobilities are denoted as $M_{B2}^{\text{dep.}}$ and $M_{B2}^{\text{indep.}}$, respectively, and those of $D0_3$-APDB are denoted as $M_{D0_3}^{\text{dep.}}$ and $M_{D0_3}^{\text{indep.}}$, respectively. For discussing the M^{sim}s for $B2$-APDB and $D0_3$-APDB regardless of the c_{v}-dependence, $M_{B2}^{\text{dep.}}$ and $M_{B2}^{\text{indep.}}$ are represented by M_{B2}^{sim}, while $M_{D0_3}^{\text{dep.}}$ and $M_{D0_3}^{\text{indep.}}$ are represented by $M_{D0_3}^{\text{sim}}$ (Table 2). When the influence of vacancy segregation is negligible, $M_{B2}^{\text{dep.}}$ and $M_{D0_3}^{\text{dep.}}$ become close to $M_{B2}^{\text{indep.}}$ and $M_{D0_3}^{\text{indep.}}$ respectively. $M_{B2}^{\text{dep.}}$ is larger than $M_{B2}^{\text{indep.}}$ by a factor of approximately up to 1.6 because of the enhancement of ordering mobility by the vacancy segregation, but both of them are smaller than $M_{\eta_{B2}}^{\text{intrinsic}}$ in the whole temperature range investigated. The difference between the M_{B2}^{sim} and the $M_{\eta_{B2}}^{\text{intrinsic}}$ is anticipated to result from solute-drag. The pink solid circle (gray solid circle in a grayscale copy) at 673 K indicates the M_{B2}^{sim} for the case where c_{Al} and c_{v} are fixed at bulk equilibrium values and only η_1, $\eta_{2\text{p}}$ and $\eta_{2\text{n}}$ are allowed to vary so that the segregation of solute atoms and the resultant solute-drag are prevented. The good agreement between the $M_{B2}^{\text{dep.}}$ and the $M_{\eta_{B2}}^{\text{intrinsic}}$ for the case of fixed c_{Al} and c_{v} supports the validity of the estimation of intrinsic boundary mobilities by the Allen-Cahn theory using Eq. (10). The differences between the $M_{\eta_{B2}}^{\text{intrinsic}}$ and the M_{B2}^{sim} decrease with increasing temperature approaching the $A2/B2$ transition temperature ($T_{\text{c}}^{A2/B2}$) of 1033 K. This is likely because the solute segregation decreases with increasing temperature as shown in the companion paper [12].

In the cases of $D0_3$-APDBs, steady-state migration with constant Ms was not obtained at

temperatures except for 673 K because the APDs vanished before the breakaway was completed as shown in Fig.5b for example. Therefore, the $M_{D0_3}^{\text{indep.}}$s and the $M_{D0_3}^{\text{dep.}}$s for the case of $r = 5$ nm are plotted as a representative mobility value in Fig. 8. The r of 5 nm was chosen simply because it is an intermediate value in the simulation. No significant difference is observed between $M_{D0_3}^{\text{indep.}}$ and $M_{D0_3}^{\text{dep.}}$. This is because of the rather weak vacancy segregation at $D0_3$-APDBs. The $M_{D0_3}^{\text{indep.}}$and $M_{D0_3}^{\text{dep.}}$ are smaller than the $M_{\eta_{D0_3}}^{\text{intrinsic}}$ in the temperature range investigated except at 673 K where the breakaway of APDB from the solute segregation atmosphere occurred before the r became 5 nm. Both $M_{D0_3}^{\text{indep.}}$and $M_{D0_3}^{\text{dep.}}$ are very close to the $M_{\eta_{D0_3}}^{\text{intrinsic}}$ at 673 K. The M calculated for the case of $\beta_{\text{Al}} = \beta_{\text{v}} = 0$ is also close to the $M_{\eta_{D0_3}}^{\text{intrinsic}}$ at 673K. This strongly implies that the difference between the $M_{D0_3}^{\text{sim.}}$ and the $M_{\eta_{D0_3}}^{\text{intrinsic}}$ before the breakaway at 673 K (Fig.5a) is due to the solute-drag, and no significant drag-force is exerted on the $D0_3$-APDB after breakaway. Also, the differences between $M_{D0_3}^{\text{sim.}}$ and the $M_{\eta_{D0_3}}^{\text{intrinsic}}$ observed at temperatures above 673 K are considered to arise because the breakaway is not completed. Although the clear breakaway and subsequent plateau was observed only for the $D0_3$-APDB at 673 K in the present study, further examples of breakaway have been observed in other cases with nonstoichiometric compositions (not shown in this paper). A clearer transition from a constant low-M regime to a constant high-M regime is observed for $D0_3$-APDB in Fe-28at%Al at 673 K, for instance. The M after the breakaway in that case is also very close to the $M^{\text{intrinsic}}$, and supports further the idea of an intrinsic boundary mobility of Allen-Cahn theory [24]. Those results will appear in a future paper on the composition dependence of segregation-affected migration of APDBs.

The Ms measured by in-situ TEM are larger than those given by the simulation by a factor of 10−40 for $D0_3$-APDB and 60−100 for $B2$-APDB as indicated in Fig. 8. The reason for the difference between the experimental data and the calculation results are unclear. Possible reasons for the difference are, (i) boundary migrations were accelerated by the vacancies introduced by

electron irradiation [34] during the in-situ TEM observation of shrinking APDBs for experimental measurement of the *M*s, (ii) the boundary migrations were accelerated by electron irradiation induced diffusion [35] and/or (iii) the extrapolation of the temperature dependence of ordering mobilities experimentally measured at 638 K and 653 K to the higher temperatures where the *in-situ* observation was carried out is beyond the limit of reasonable approximation. The exact reason will probably be elucidated by comparing 3D simulation and APD growth in a bulk Fe_3Al which is not affected by the electron irradiation.

Intending to quantify the effect of solute drag on the migration of *B*2-APDB, calculations were performed using Cahn's theory of solute drag [14]. In the calculation, a linear velocity/driving-force relation was used. Although the relation is known to be inadequate to describe intrinsic migration of APDBs [24] for temperatures near T_c, it is valid at temperatures far below T_c such as 673 K. First, extrinsic boundary mobilities ($M^{\text{extrinsic}}$) were defined as coefficients which relate the boundary velocity (V) and APD radius r for the case where the drag-force is neglected. Fig. 9 compares the $M_{\eta_{B2}}^{\text{intrinsic}}$, $M_{\eta_{B2}}^{\text{extrinsic}}$ and M_{B2}^{sim} at 673 K for both cases of c_v-dependent (Fig. 9a) and c_v-independent (Fig. 9b) phase-field mobilities. The $M_{\eta_{B2}}^{\text{intrinsic}}$s were calculated by using Eq. (10), while the $M_{\eta_{B2}}^{\text{extrinsic}}$s were evaluated as follows.

For taking into account the drag-force, it is convenient to define another boundary mobility m which relates the boundary velocity and driving pressure (P) applied to the migrating boundary by

$$V = mP \tag{11}$$

Hereafter, the simbol m is used to represent pressure driven intrinsic boundary mobility to distinguish it from the intrinsic boundary mobility $M^{\text{intrinsic}}$. In the case of shrinking 2D circular APD, P is given by

$$P = \sigma_{\text{APDB}}/r - P^{\text{drag}} \tag{12}$$

where σ_{APDB} is the interface energy of the APDB and P^{drag} is the drag force.

Substituting Eq. (12) into Eq. (11),

$$V = m(\sigma_{\mathrm{APDB}}/r - P^{\mathrm{drag}}). \tag{13}$$

When there is no drag force (i.e. P^{drag}=0), V can be determined by $M^{\mathrm{intrinsic}}$ and curvature as [24]

$$V = M^{\mathrm{intrinsic}}/r, \tag{14}$$

and Eq. (13) becomes

$$V = m(\sigma_{\mathrm{APDB}}/r) \tag{15}$$

Comparing Eq. (14) and Eq. (15) gives

$$M^{\mathrm{intrinsic}} = m\sigma_{\mathrm{APDB}}. \tag{16}$$

Here we define a new parameter named extrinsic boundary mobility $M^{\mathrm{extrinsic}}$ which relates the curvature $1/r$ and V without regard to the drag force as

$$V = M^{\mathrm{extrinsic}}/r. \tag{17}$$

Note that Eq. (17) can be used only when P^{drag} is non-zero while Eq. (14) holds only when P^{drag} is zero. Comparing Eq. (13) and Eq. (17) gives

$$M^{\mathrm{extrinsic}} = mr(\sigma_{\mathrm{APDB}}/r - P^{\mathrm{drag}}). \tag{18}$$

By using Eq. (16), Eq. (18) can be rewritten

$$M^{\mathrm{extrinsic}} = M^{\mathrm{intrinsic}} r(\sigma_{\mathrm{APDB}}/r - P^{\mathrm{drag}})/\sigma_{\mathrm{APDB}} = M^{\mathrm{intrinsic}}(1 - rP^{\mathrm{drag}}/\sigma_{\mathrm{APDB}}) \tag{19}$$

Substituting Eq. (10) into Eq. (18)

$$M^{\mathrm{extrinsic}} = 2\kappa\alpha r/\sigma_{\mathrm{APDB}}(\sigma_{\mathrm{APDB}}/r - P^{\mathrm{drag}}) = 2\kappa\alpha(1 - rP^{\mathrm{drag}}/\sigma_{\mathrm{APDB}}) \tag{20}$$

Eq. (20) allows us to evaluate the $M^{\mathrm{extrinsic}}$ by using the σ^{APDB} and P^{drag} which can be calculated as follows. The σ_{APDB} was calculated by using the following equations.

$$\sigma_{\mathrm{APDB}} = \int_0^{+\infty} \left[\Delta f + \kappa_{\eta_1} \left| \frac{d\eta_1}{dr} \right|^2 + \kappa_{\eta_{2p}} \left| \frac{d\eta_{2p}}{dr} \right|^2 + \kappa_{\eta_{2n}} \left| \frac{d\eta_{2n}}{dr} \right|^2 \right] dr \tag{22}$$

where Δf is the energy increase due to the deviations in the order parameters from their equilibrium values and given by:

$$\Delta f = \Delta F(c\ ,\eta_1,\eta_{2p},\eta_{2n}) - \left[\Delta F\ (c_0,\eta_{10},\eta_{2p0},\eta_{2n0}) + (c-c_0)\cdot\left.\frac{\partial F}{\partial c}\right|_{\substack{c=c_0\\ \eta_1=\eta_{10}\\ \eta_{2p}=\eta_{2p0}\\ \eta_{2n}=\eta_{2n0}}} + (\eta_1-\eta_{10})\cdot\left.\frac{\partial F}{\partial \eta_1}\right|_{\substack{c=c_0\\ \eta_1=\eta_{10}\\ \eta_{2p}=\eta_{2p0}\\ \eta_{2n}=\eta_{2n0}}} + (\eta_{2p}-\eta_{2p0})\cdot\left.\frac{\partial F}{\partial \eta_{2p}}\right|_{\substack{c=c_0\\ \eta_1=\eta_{10}\\ \eta_{2p}=\eta_{2p0}\\ \eta_{2n}=\eta_{2n0}}} + (\eta_{2n}-\eta_{2n0})\cdot\left.\frac{\partial F}{\partial \eta_{2n}}\right|_{\substack{c=c_0\\ \eta_1=\eta_{10}\\ \eta_{2p}=\eta_{2p0}\\ \eta_{2n}=\eta_{2n0}}}\right] \quad (23)$$

P^{drag} was evaluated from the profile of diffusion potential of Al-atoms, $\delta F/\delta c_{\mathrm{Al}}$ by

$$P^{\mathrm{drag}} = -\int_0^{+\infty}\left[\left(c_{\mathrm{Al}}(r)-c_{\mathrm{Al}}^{\mathrm{eq}}\right)\frac{d}{dr}\left(\frac{\delta F}{\delta c_{\mathrm{Al}}}\right)\right]dr \quad (24)$$

where $c_{\mathrm{Al}}^{\mathrm{eq}}$ is the Al concentration of the alloy [14]. Note that Eqs. (23) and (24) result in a dependence of σ_{APDB} and P^{drag}, and hence $M^{\mathrm{extrinsic}}$, on radius r.

$M^{\mathrm{extrinsic}}$s of $B2$-APDB ($M_{\eta_{\mathrm{B2}}}^{\mathrm{extrinsic}}$) calculated by using Eq. (21) are shown in Fig. 9a and Fig. 9b for the cases of c_{v}-dependent and c_{v}-independent cases, respectively. The $M_{\eta_{\mathrm{B2}}}^{\mathrm{intrinsic}}$ estimated by the Allen-Cahn's theory, $2\kappa\alpha$, and the M_{B2}^{sim} are also indicated for comparison. The M_{B2}^{sim}s are much smaller than the $M_{\eta_{\mathrm{B2}}}^{\mathrm{intrinsic}}$s and closer to the $M_{\eta_{\mathrm{B2}}}^{\mathrm{extrinsic}}$s in both of c_{v}-dependent and c_{v}-independent cases. However, the M_{B2}^{sim}s are significantly larger than the $M_{\eta_{\mathrm{B2}}}^{\mathrm{extrinsic}}$s especially in the case of c_{v}-dependent phase-field mobility. The most probable reason is the inappropriate application of Cahn's solute-drag theory [14] to APDB migration. In the Cahn's theory, steady-state migration of a planar grain boundary is considered. On the other hand, in our study, migration of APDBs associated with shrinking circular APDs are considered, and therefore the APDB migration is not in a steady state. As indicated in Fig. 6a, the Al concentrations inside and outside of the APD become higher and lower, respectively, as the APDs shrink. In such a situation, the P^{drag} evaluated by Eq. (14) in which the $c_{\mathrm{Al}}^{\mathrm{eq}}$ is assumed to be constant, cannot be estimated correctly. In addtion, in the case of c_{v}-dependent phase-field mobilities, the increase in the moblities due to the vacancy segregation makes the difference larger. Actually, the difference between the M_{B2}^{sim} and the $M_{\eta_{\mathrm{B2}}}^{\mathrm{extrinsic}}$

is larger in the c_v-dependent case (Fig.9a) than in the c_v-independent case (Fig.9b). Further study for evaluating the drag-force for boundary migrations at unsteady states is in progress.

5. Conclusion

Effects of segregation of solute atoms and vacancies on migration of $a/4<111>$ APDB ($B2$-APDB) and $a/2<100>$ APDB ($D0_3$-APDB) in Fe_3Al were studied using the phase-field model for vacancy containing system which was developed in the previous study. Important findings of the present study are:

1. Solute atmospheres follow shrinking $a/4<111>$ APDBs until the APD vanishes by shrinking to zero radius. The boundary mobilities are smaller than the intrinsic boundary mobilities because of the solute-drag effect.
2. The boundary mobilities of $a/4<111>$ APDBs can be enhanced by a factor of up to 60 % by vacancy segregation in the temperatures above 673 K whereas those of $a/2<100>$ APDBs are enhanced by only a few percent.
3. $a/2<100>$ APDBs break away from solute atmospheres during the course of the shrinking in contrast with $a/4<111>$ APDB. The $a/2<100>$ APDB boundary mobilities increase by a factor of up to 40 % accompanying the breakaway and become equal to the intrinsic boundary mobilities even though some depletion and segregation of solute Al-atoms remained ahead and behind the migrating APDB, respectively.
4. The boundary mobility of $a/2<100>$ APDB after breakaway from the solute atmosphere is in good agreement with the intrinsic boundary mobility evaluated from the Allen-Cahn theory.

Acknowledgement

The present work was supported by the "Overseas Advanced Educational Research Practice Support Program" of the Japan Ministry of Education, Culture, Sports, Science and Technology (MEXT) and partly supported by Yamada Science Foundation. We would like to express our sincere appreciation to Professor W. Craig Carter for access to his lab's efficient computation environment and his support for conducting this work. We greatly appreciate Dr. Toshiyuki Koyama for providing the program code on which the simulation of this study is based.

Appendix

Description of free energy of vacancy containing Fe_3Al by Bragg-Williams approximation

Site occupations in the $D0_3$ ordered structure are defined using the 4-sublattices as follows,

$$\eta_1 = \left(\frac{p_{\mathrm{Al}}^{\alpha} + p_{\mathrm{Al}}^{\beta}}{2} - \frac{p_{\mathrm{Al}}^{\gamma} + p_{\mathrm{Al}}^{\delta}}{2} \right) \Big/ 2 \tag{A1}$$

$$\eta_2 = \begin{cases} \dfrac{p_{\mathrm{Al}}^{\alpha} - p_{\mathrm{Al}}^{\beta}}{2} \equiv \eta_{2\mathrm{p}} & (\eta_1 > 0) \\ \dfrac{p_{\mathrm{Al}}^{\gamma} - p_{\mathrm{Al}}^{\delta}}{2} \equiv \eta_{2\mathrm{n}} & (\eta_1 < 0) \end{cases} \tag{A2}$$

where p_{Al}^{i} (i = α, β, γ, δ) are the occupation probabilities of Al atoms on each sublattice. We define the $D0_3$-LRO for positive and negative $B2$-LRO as $\eta_{2\mathrm{p}}$ and $\eta_{2\mathrm{n}}$, respectively. The average site fraction of Al atoms in the whole crystal ($\bar{x}_{\mathrm{Al}}$) is given by

$$\bar{x}_{\mathrm{Al}} = \frac{1}{4}\left(p_{\mathrm{Al}}^{\alpha} + p_{\mathrm{Al}}^{\delta} + p_{\mathrm{Al}}^{\gamma} + p_{\mathrm{Al}}^{\beta} \right). \tag{A3}$$

By solving Eqs. (A1) – (A3) simultaneously, the Al occupation probabilities on each site can be expressed as follows:

$$
\begin{aligned}
p_{\mathrm{Al}}^{\alpha} &= x_{\mathrm{Al}} + \eta_{1} + \eta_{2\mathrm{p}} \\
p_{\mathrm{Al}}^{\beta} &= x_{\mathrm{Al}} + \eta_{1} - \eta_{2\mathrm{p}} \\
p_{\mathrm{Al}}^{\gamma} &= x_{\mathrm{Al}} - \eta_{1} + \eta_{2\mathrm{n}} \\
p_{\mathrm{Al}}^{\delta} &= x_{\mathrm{Al}} - \eta_{1} - \eta_{2\mathrm{n}}
\end{aligned}
\tag{A4}
$$

The free energy of the system in the Bragg-Williams approximation [33] is given by:

$$
\begin{aligned}
\Delta F = \frac{N}{2}\Big\{ & V(0)x_{\mathrm{Al}}(1-x_{\mathrm{Al}}) + V(\vec{k}_1)\eta_1{}^2 + \frac{1}{2}V(\vec{k}_2)\eta_{2\mathrm{p}}{}^2 + \frac{1}{2}V(\vec{k}_2)\eta_{2\mathrm{n}}{}^2 \Big\} \\
& + k_{\mathrm{B}}T\{\, p_{\mathrm{Al}}^{\alpha}\ln p_{\mathrm{Al}}^{\alpha} + (1-p_{\mathrm{Al}}^{\alpha})\ln(1-p_{\mathrm{Al}}^{\alpha}) + p_{\mathrm{Al}}^{\beta}\ln p_{\mathrm{Al}}^{\beta} + (1-p_{\mathrm{Al}}^{\beta})\ln(1-p_{\mathrm{Al}}^{\beta}) \\
& \quad + p_{\mathrm{Al}}^{\gamma}\ln p_{\mathrm{Al}}^{\gamma} + (1-p_{\mathrm{Al}}^{\gamma})\ln(1-p_{\mathrm{Al}}^{\gamma}) + p_{\mathrm{Al}}^{\delta}\ln p_{\mathrm{Al}}^{\delta} + (1-p_{\mathrm{Al}}^{\delta})\ln(1-p_{\mathrm{Al}}^{\delta}) \,\}
\end{aligned}
\tag{A5}
$$

where N is the number of atoms in the system and $V(\vec{k}_s)$ are the Fourier transforms of real-space pair-interaction energies, $v(\vec{r})$, expressed as:

$$
V(\vec{k}_s) = \sum v(\vec{r})\exp(-i\vec{k}_s\cdot\vec{r}) \tag{A6}
$$

where $\vec{k}_s$ is a reciprocal lattice vector and $v(\vec{r})$ is defined by:

$$
v(\vec{r}) = \varepsilon_{\mathrm{FeFe}}^{r} + \varepsilon_{\mathrm{AlAl}}^{r} - 2\varepsilon_{\mathrm{FeAl}}^{r} \tag{A7}
$$

where $\varepsilon_{\mathrm{FeFe}}^{\mathrm{r}}$, $\varepsilon_{\mathrm{AlAl}}^{\mathrm{r}}$ and $\varepsilon_{\mathrm{FeAl}}^{\mathrm{r}}$ are energies of Fe-Fe, Al-Al and Fe-Al bonds of distance r, respectively. The values of $V(\vec{k}_s)$ used were those determined from order-disorder transition temperatures of stoichiometric Fe_3Al in the experimental phase diagram [33]*.

When vacancies are regarded as the third component, the site-fraction of Al atoms $\bar{x}_{\mathrm{Al}}$ is given by

$$
x_{\mathrm{Al}} = c_{\mathrm{Al}}(1-c_{\mathrm{V}}) \tag{A8}
$$

where c_{Al} is the Al atom fraction of the alloy and c_{V} is the number fraction of vacancies.

We assume that vacancies occupy only Fe-sites which have first nearest neighbor Al atoms in the

* The $V(\vec{k}_s)$ values were assumed independent of composition to simplify interpretation of trends in the results.

perfect $D0_3$-ordered structure, consistent with the preferential occupation of vacancies revealed by Mössbauer spectroscopy [36]. Then, the probabilities of finding vacancies on α, β, γ and δ sites are defined as follows:

when $-0.25 \le \eta_1 \le 0.25$

$$p_v^{\alpha} = c_V\left(1 - \frac{\eta_1}{0.25}\right) \quad \text{(A9)}$$

$$p_v^{\beta} = c_V\left(1 - \frac{\eta_1}{0.25}\right) \quad \text{(A10)}$$

$$p_v^{\gamma} = c_V\left(1 + \frac{\eta_1}{0.25}\right) \quad \text{(A11)}$$

$$p_v^{\delta} = c_V\left(1 + \frac{\eta_1}{0.25}\right) \quad \text{(A12)}$$

Where c_{Al} is larger than 0.25, η_1 can be larger than 0.25 or smaller than 0.25 and then Eqs. (A9) –(A12) cannot be used for defining the vacancy occupation probabilities, p_v^i (i=α, β, δ, γ). For those cases, p_v^is are defined as follows

When $\eta_1 > 0.25$

$$p_v^{\alpha} = p_v^{\beta} = 0 \text{ and } p_v^{\gamma} = p_v^{\delta} = 2c_V \quad \text{(A13)}$$

When $\eta_1 <$ - 0.25

$$p_v^{\alpha} = p_v^{\beta} = 2c_V \text{ and } p_v^{\gamma} = p_v^{\delta} = 0 \quad \text{(A14)}$$

Probabilities of finding an Fe atom on an *i*-site (*i* = α, β, γ and δ) are given by:

$$p_{Fe}^i = 1 - p_{Al}^i - p_v^i \quad \text{(A15)}$$

Then, configurational entropy of the assembly of atoms and vacancies is given by:

$$S = -\frac{k_B}{4} \sum_{i=\alpha,\beta,\gamma,\delta} \left\{ \sum_{k=\mathrm{Al,Fe,v}} \left(p_k^i \ln p_k^i \right) \right\} \quad \text{(A16)}$$

Assuming that vacancy formation enthalpy (H_f) is independent of degree of order, the enthalpy is given by

$$H = H_{NV} + c_v H_f \quad \text{(A17)}$$

where H_{NV} is the enthalpy of a vacancy-free crystal and H_F is the vacancy formation enthalpy.

References

[1] Maziasz PJ, Liu CT, Goodwin, Overview of the development of FeAl intermetallic alloys, In: the 2nd International Conference on Heat-Resistant Materials, Gatlinburg, Tennessee, 1995.

[2] Swann PR, Dufff WR, Fisher RM, Trans AIME 1969;245:851.

[3] Yoshimi K, Terashima H, Hanada S, Mater Sci Eng A 1995;194:53.

[4] Koizumi Y, Minamino Y, Tsuji N, Nakano T, Umakoshi Y, Mat Res Soc Symp 2003;753:267.

[5] Koizumi Y, Minamino Y, Nakano T, Umakoshi Y, Philos Mag 2008;88:45.

[6] Yasuda HY, Nakano K, Nakajima T, Ueda M, Umakoshi Y, Acta mater 2003;51:5101.

[7] Yasuda HY, Nakajima T, Umakoshi Y, Intermetallics 2007;15:819.

[8] Yasuda HY, Nakajima T, Umakoshi Y, Scripta Mater 2006;55:859.

[9] Yasuda HY, Nakajima T, Nakano K, Yamaoka K, Ueda M, Umakoshi Y, Acta Mater. 2005;53:5343.

[10] Yasuda HY, Nakajima T, Murakami S, Ueda M, Umakoshi Y, Intermetallics 2006;14:1221.

[11] Koizumi Y, Hagiwara T, Minamino Y, Tsuji N, Mater. Res. Soc. Symp. Proc. 2005; 842:53

[12] Koizumi Y. Acta Metall. 2008;56:5861.

[13] Lücke K, Detert K, Acta Metall. 1957;5:628.

[14] Cahn JW, Acta Metall. 1962;10:789.

[15] Hillert M, Acta Metall. 1977;25:11.

[16] Hillert M, Acta Mater. 1999;47:4481.

[17] Cha PR, Kim SG, Yeon DH, Yoon JK, Acta Mater. 2002;50:3817.

[18] Hillert M, Acta Mater. 2004;52:5289.

[19] Mendelev MI, Srolovits DJ, Acta Mater. 2001;49:589.

[20] Kim SG, Park YB, Acta Mater 2008;56:3739.

[21] Krzanowski JE, Allen SM, Acta Metall. 1986;34:1035.

[22] Krzanowski JE, Allen SM, Acta Metall. 1986;34:1045.

[23] Cahn JW, JE Hilliard. 1958;28:258.

[24] Allen SM, Cahn JW, Acta Metall. 1979;27:1085.

[25] Balluffi RW, Allen SM, Carter WC, Kinetics of Materials, Wiley 2005, p 52 (for Nernst-Einstein equation), p.378 (for parabolic growth law).

[26] Salamon M, Mehrer H, Z Metallk, 2005;96:833.

[27] Schaefer HE, Würschum R, Sob M, Zak T, Yu WZ, Eckert W, Banhart F, Phys. Rev. B 1990;41:11869.

[28] Wolff J, Franz M, Broska A, Köhler B, Hehenkamp Th, Mat Sci Eng A 1997; 239-240:213.

[29] Kirkaldy JS, J. Appl. Phys., 1998;83:5773.

[30] Hillert M, Acta Mater. 2001;49:2491.

[31] Oki K, Masuda J, Hasaka M, Trans. JIM, 1975;39:589. (in Japanese)

[32] Park BW, Stephenson GB, Allen SM, Ludwig KF Jr., Phys. Rev. Lett. 1992;68:1742.

[33] Park W, Ph D thesis, Migration Kinetics of Antiphase Boundaries in Fe-Al Ordered Alloys, Department of Materials Science and Engineering, Massachusetts Institute of Technology, Boston, 1988.

[34] Makin MJ, Philos. Mag. 1968;18:637.

[35] Kiritani M, J. Phys. Soc. Japan 1976;40:1035.

[36] Jiraskova Y, Schneeweiss O, Sob M, Novotny I, Prochazka I, Becvar F, et al. J Phys IV Colloq C1, supplement au J Phys III 1995:5.

Figure captions

Fig. 1 Snap shots of LRO field (a-d), Al concentration field (e-h) and vacancy concentration field (i-l) around *B*2-type *a*/4<111> APD shrinking at 673 K. The time from the beginning of the simulation are 0 s (a, e, i), 500 ks (b, f, j), 750 ks (c, g, k) and 1000 ks (d, h, l).

Fig. 2 Snap shots of LRO field (a-d), Al concentration field (e-h) and vacancy concentration field (i-l) around $D0_3$-type *a*/2<100> APD shrinking at 673 K. The time from the beginning of the simulation are 0 ks (a, e, i), 30 ks (b, f, j), 50 ks (c, g, k) and 70 ks (d, h, l).

Fig. 3 Radii of shrinking circular APDs as a function of annealing time at 673 K; (a) time range up to 1.7×10^6 s, (b) time range up to 6×10^4 s.

Fig. 4 Boundary velocities of circular shrinking APDBs as a function APDB curvature ($1/r$); (a) boundary velocity range up to 7×10^{-4} nm/s; (b) boundary velocity range up to 5×10^{-5} nm/s.

Fig. 5 Boundary mobilities of circular APDBs shrinking at (a) 673 K and (b) 773 K as a function of APD radius (r). Insets are the magnifications of the curves for *B*2-APDBs.

Fig. 6 Profiles of (a) *B*2-LRO, (b) Al concentration and (c) vacancy concentration across circular *a*/4<111>APDBs shrinking at 673 K with diameters of 11.2 nm, 10 nm, 5 nm and 2 nm.

Fig. 7 Profiles of (a) $D0_3$-LRO, (b) Al concentration and (c) vacancy concentration across circular *a*/2<100>APDBs shrinking at 673 K with diameters of 11.2 nm, 10 nm, 5 nm and 2 nm.

Fig. 8 Boundary mobilities of shrinking APDs as a function of temperature. The boundary mobilities evaluated from the simulation results are compared with intrinsic boundary mobilities and those evaluated from in-situ TEM of observation [32].

Fig. 9 Comparison of simulated boundary moblities, intrinsic boundary mobilities and extrinsic boundary mobilities of *B*2-APDB at 673 K for the cases of (a) c_v-dependent and (b) c_v-independent phase field mobilities.

Table 1 Diffusivity and ordering mobility data used in the calculations.

Parameter	Value	Al concentration	Reference
$\tilde{D}_0$	1.2×10^{-1} m^2/s	25.5 at%	Salamon [26]
Q_{int}	279 kJ mol^{-1}	25.5 at%	Salamon [26]
S_F	$5k_B$	23.7 at%	Schaefer et al. [27]
H_F	89 kJ mol^{-1}	23.7 at%	Wolff et al. [28]
$\alpha_{\eta_{B2}}$	3.12×10^{3} m^{3}J^{-1}s^{-1}	24.9 at%	Oki et al. [29]
$Q_{\eta_{B2}}$	193 kJ mol^{-1}	24.9 at%	Oki et al. [29]
$\alpha_{\eta_{D0_3}}$	3.12×10^{4} m^{3}J^{-1}s^{-1}	24.9 at%	Oki et al. [29]
$Q_{\eta_{D0_3}}$	193 kJ mol^{-1}	24.9 at%	Oki et al. [29]

$$\tilde{D}(T) = \tilde{D}_0 \exp\left(-Q_{\text{int}}/RT\right)$$

Table 2 Classification of phase-field mobilities and boundary mobilities

Mobility	Regardless of LRO	LRO	Regardless of c_v-dependence	c_v-dependent	c_v-independent
Phase field mobility	ordering mobility α	$B2$	$\alpha_{\eta_{B2}}$	$\alpha_{\eta_{B2}}^{\text{dep.}}$	$\alpha_{\eta_{B2}}^{\text{indep.}}$
		$D0_3$	$\alpha_{\eta_{D0_3}}$	$\alpha_{\eta_{D0_3}}^{\text{dep.}}$	$\alpha_{\eta_{D0_3}}^{\text{indep.}}$
	Al atom mobility β_{Al}	–	–	$\beta_{\text{Al}}^{\text{dep.}}$	$\beta_{\text{Al}}^{\text{indep.}}$
	vacancy mobility β_v	–	–	–	
Boundary mobility M	intrinsic boundary mobility $M^{\text{intrinsic}}$	$B2$	$M_{\eta_{B2}}^{\text{intrinsic}}$	–	
		$D0_3$	$M_{\eta_{D0_3}}^{\text{intrinsic}}$	–	
	extrinsic boundary mobility $M^{\text{extrinsic}}$	$B2$	$M_{\eta_{B2}}^{\text{extrinsic}}$	–	–
		$D0_3$	$M_{\eta_{D0_3}}^{\text{extrinsic}}$	–	–
	simulated boundary mobility M^{sim}	$B2$	M_{B2}^{sim}	$M_{B2}^{\text{dep.}}$	$M_{B2}^{\text{indep.}}$
		$D0_3$	$M_{D0_3}^{\text{sim}}$	$M_{D0_3}^{\text{dep.}}$	$M_{D0_3}^{\text{indep.}}$
Pressure driven boundary mobility	m	$B2$	$m_{\eta_{B2}}$	–	–
		$D0_3$	$m_{\eta_{D0_3}}$	–	–

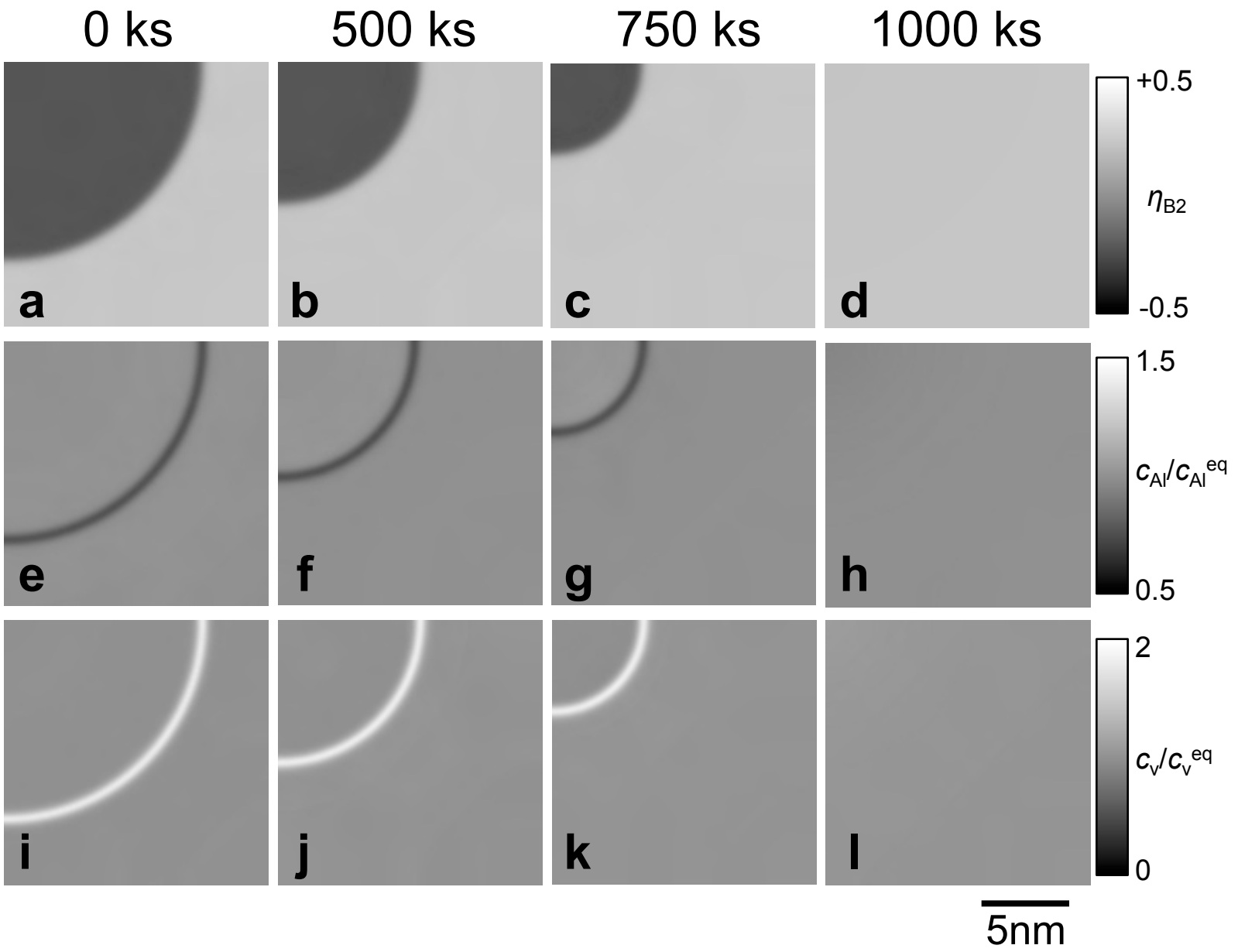
0 ks
500 ks
750 ks
1000 ks
a
b
c
d
e
f
g
h
i
j
k
l
+0.5
η_{B2}
-0.5
1.5
c_{Al}/c_{Al}^{eq}
0.5
2
c_v/c_v^{eq}
0
5nm

Fig. 1

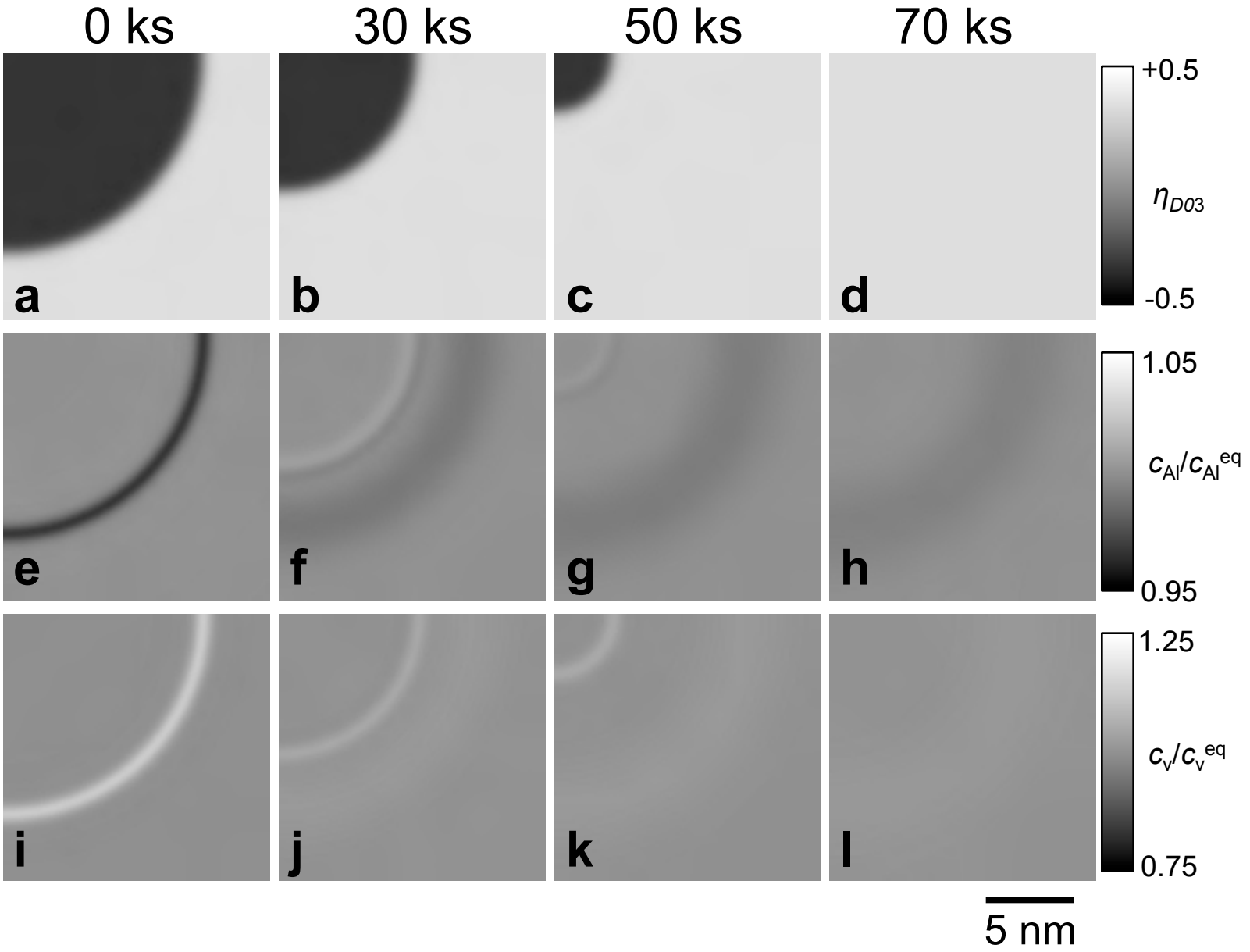
0 ks
30 ks
50 ks
70 ks
a
b
c
d
+0.5
η_{D03}
-0.5
e
f
g
h
1.05
c_{Al}/c_{Al}^{eq}
0.95
i
j
k
l
1.25
c_v/c_v^{eq}
0.75
5 nm

Fig. 2

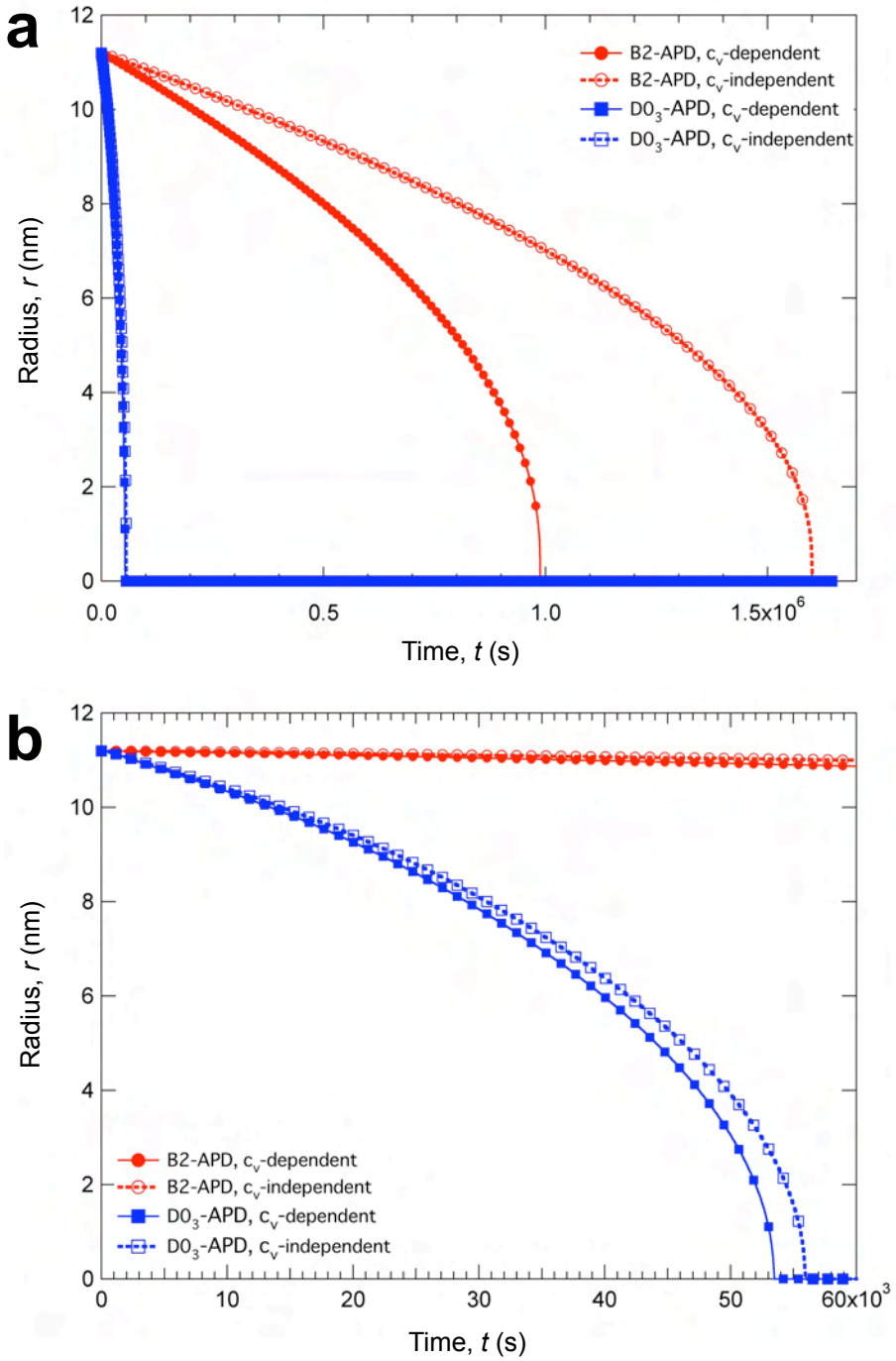
a
Radius, r (nm)
Time, t (s)
B2-APD, c_v-dependent
B2-APD, c_v-independent
D0_3-APD, c_v-dependent
D0_3-APD, c_v-independent
0
2
4
6
8
10
12
0.0
0.5
1.0
1.5x10^6
b
Radius, r (nm)
Time, t (s)
B2-APD, c_v-dependent
B2-APD, c_v-independent
D0_3-APD, c_v-dependent
D0_3-APD, c_v-independent
0
2
4
6
8
10
12
0
10
20
30
40
50
60x10^3

Fig.3

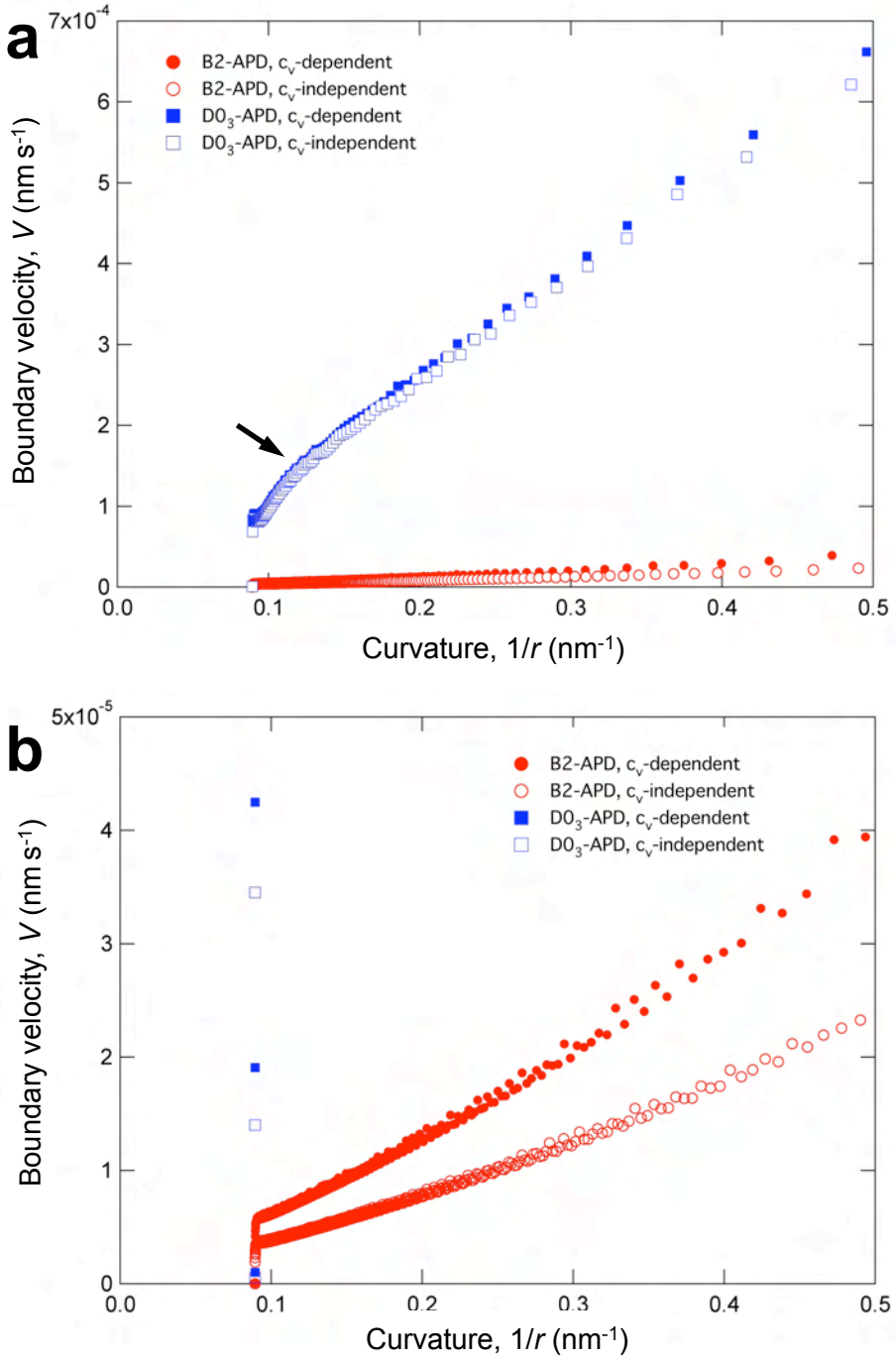
a
7x10^-4
B2-APD, c_v-dependent
B2-APD, c_v-independent
DO_3-APD, c_v-dependent
DO_3-APD, c_v-independent
Boundary velocity, V (nm s^-1)
Curvature, 1/r (nm^-1)
b
5x10^-5
B2-APD, c_v-dependent
B2-APD, c_v-independent
DO_3-APD, c_v-dependent
DO_3-APD, c_v-independent
Boundary velocity, V (nm s^-1)
Curvature, 1/r (nm^-1)

Fig.4

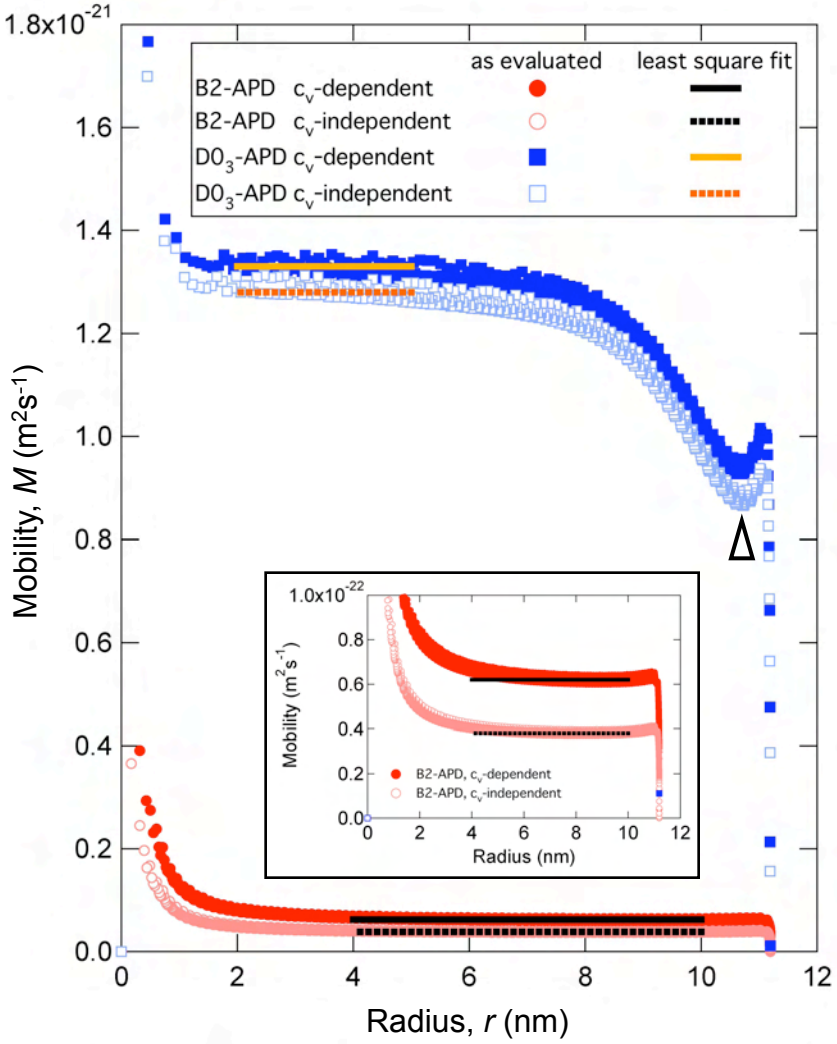
1.8x10^-21
Mobility, M (m²s⁻¹)
as evaluated
least square fit
B2-APD c_v-dependent
B2-APD c_v-independent
DO3-APD c_v-dependent
DO3-APD c_v-independent
Δ
1.0x10^-22
Mobility (m²s⁻¹)
B2-APD, c_v-dependent
B2-APD, c_v-independent
Radius (nm)
Radius, r (nm)

a

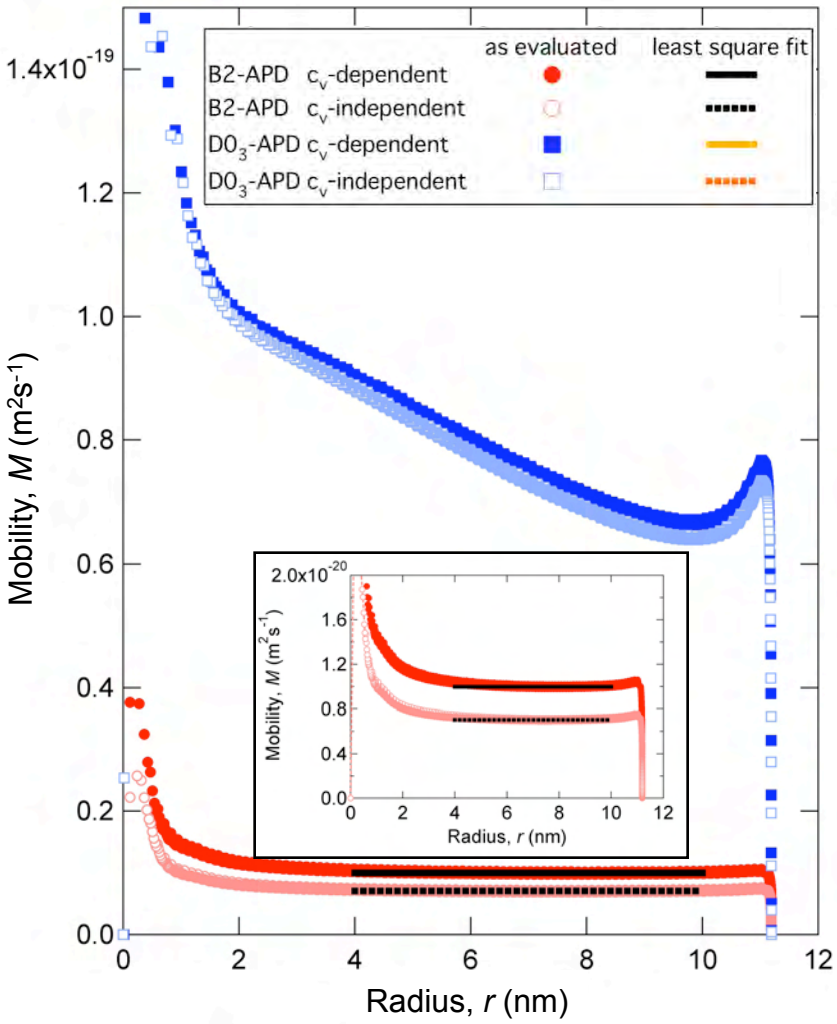
1.4x10^-19
Mobility, M (m²s⁻¹)
as evaluated
least square fit
B2-APD c_v-dependent
B2-APD c_v-independent
DO3-APD c_v-dependent
DO3-APD c_v-independent
2.0x10^-20
Mobility, M (m²s⁻¹)
Radius, r (nm)
Radius, r (nm)

b

Fig.5

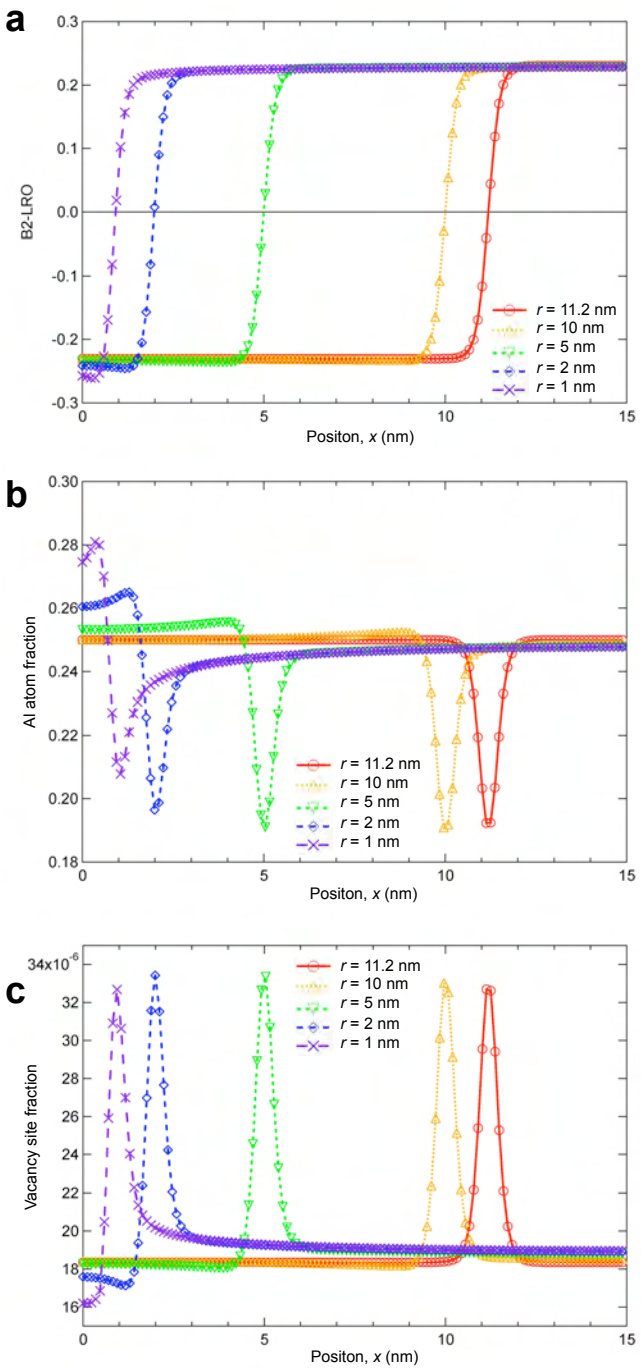
a
B2-LRO
Positon, x (nm)
r = 11.2 nm
r = 10 nm
r = 5 nm
r = 2 nm
r = 1 nm
b
Al atom fraction
Positon, x (nm)
c
34x10-6
Vacancy site fraction
Positon, x (nm)

Fig. 6

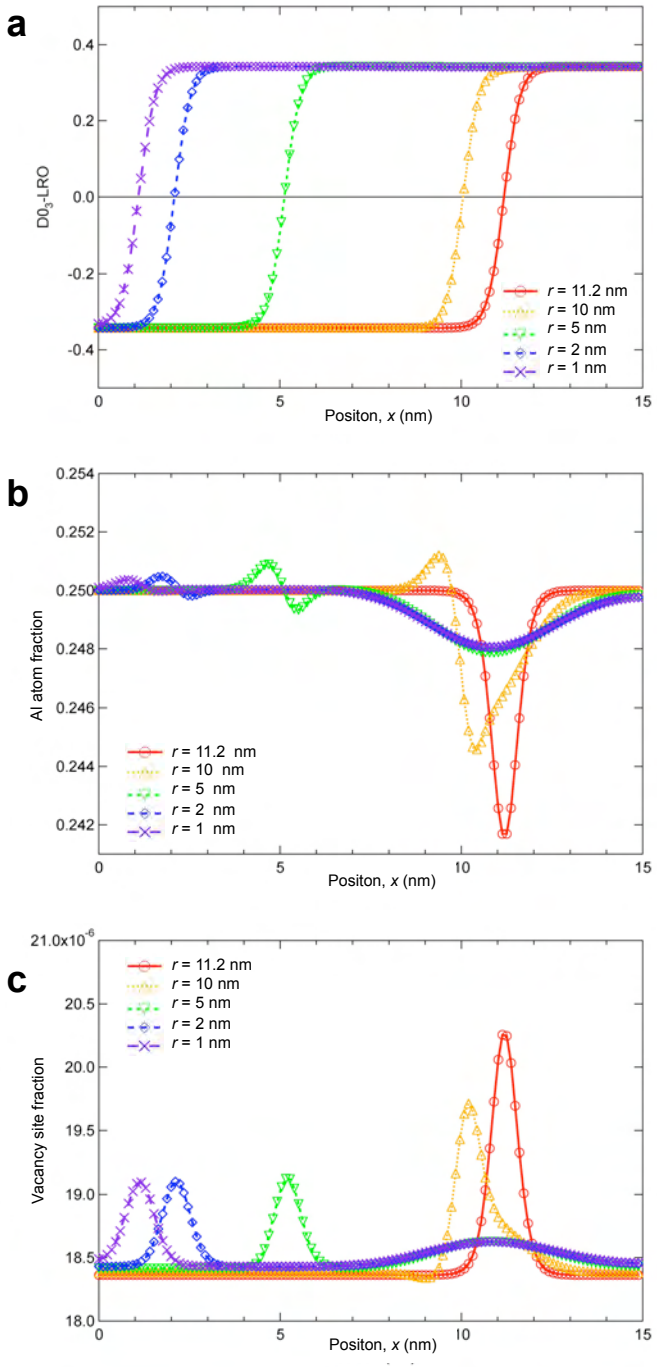
a
0.4
0.2
0.0
-0.2
-0.4
$D0_3$-LRO
0
5
10
15
Positon, x (nm)
r = 11.2 nm
r = 10 nm
r = 5 nm
r = 2 nm
r = 1 nm
b
0.254
0.252
0.250
0.248
0.246
0.244
0.242
Al atom fraction
0
5
10
15
Positon, x (nm)
r = 11.2 nm
r = 10 nm
r = 5 nm
r = 2 nm
r = 1 nm
c
21.0x10-6
20.5
20.0
19.5
19.0
18.5
18.0
Vacancy site fraction
0
5
10
15
Positon, x (nm)
r = 11.2 nm
r = 10 nm
r = 5 nm
r = 2 nm
r = 1 nm

Fig. 7

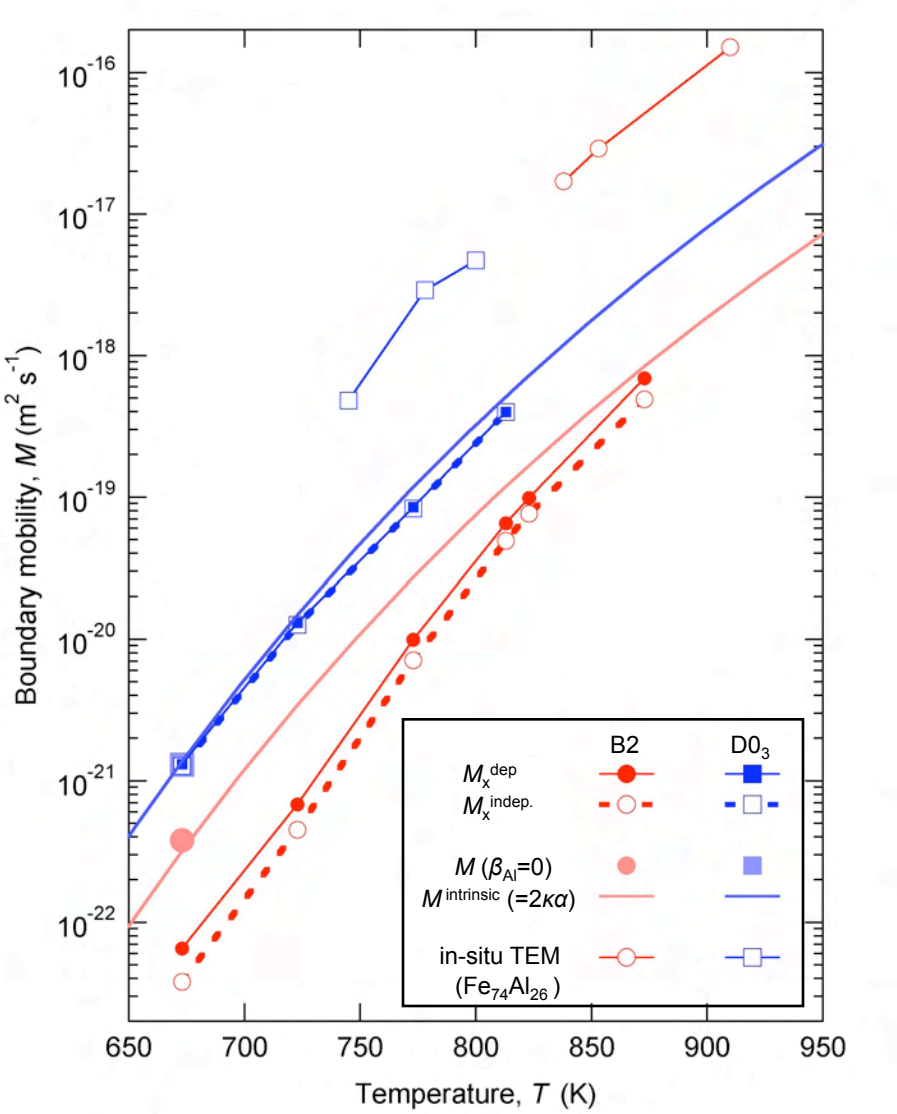
Boundary mobility, M (m2 s-1)
10-16
10-17
10-18
10-19
10-20
10-21
10-22
650
700
750
800
850
900
950
Temperature, T (K)
B2
D03
Mxdep
Mxindep.
M (βAl=0)
M intrinsic (=2κα)
in-situ TEM
(Fe74Al26)

Fig.8

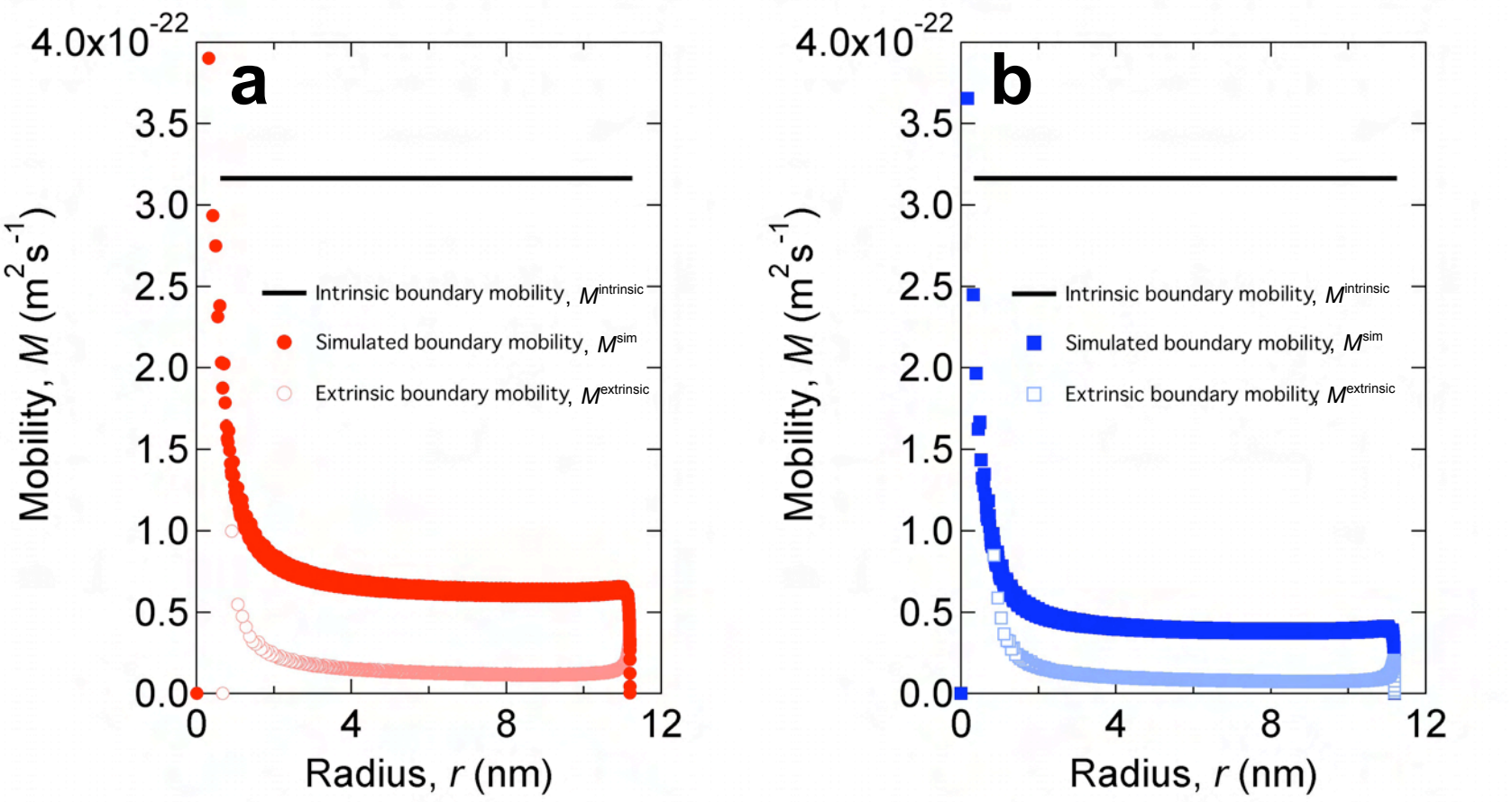
a
b
4.0x10^-22
3.5
3.0
2.5
2.0
1.5
1.0
0.5
0.0
0
4
8
12
Mobility, M (m^2 s^-1)
Radius, r (nm)
Intrinsic boundary mobility, M^intrinsic
Simulated boundary mobility, M^sim
Extrinsic boundary mobility, M^extrinsic

Fig. 9